



**HAL**  
open science

## Direct measurement of alpha emission probabilities in the decay of $^{226}\text{Ra}$

M. Marouli, S. Pommé, R. van Ammel, E. García-Toraño, T. Crespo, Sylvie  
Pierre

► **To cite this version:**

M. Marouli, S. Pommé, R. van Ammel, E. García-Toraño, T. Crespo, et al.. Direct measurement of alpha emission probabilities in the decay of  $^{226}\text{Ra}$ . *Applied Radiation and Isotopes*, 2017, 125, pp.196-202. 10.1016/j.apradiso.2017.04.029 . cea-04550224

**HAL Id: cea-04550224**

**<https://cea.hal.science/cea-04550224>**

Submitted on 17 Apr 2024

**HAL** is a multi-disciplinary open access archive for the deposit and dissemination of scientific research documents, whether they are published or not. The documents may come from teaching and research institutions in France or abroad, or from public or private research centers.

L'archive ouverte pluridisciplinaire **HAL**, est destinée au dépôt et à la diffusion de documents scientifiques de niveau recherche, publiés ou non, émanant des établissements d'enseignement et de recherche français ou étrangers, des laboratoires publics ou privés.

# Direct measurement of alpha emission probabilities in the decay of $^{226}\text{Ra}$

M. Marouli<sup>1</sup>, S. Pommé<sup>\*1</sup>, R. Van Ammel<sup>1</sup>, E. García-Toraño<sup>2</sup>, T. Crespo<sup>2</sup>, S. Pierre<sup>3</sup>

<sup>1</sup> *European Commission, Joint Research Centre, Directorate for Nuclear Safety and Security, Retieseweg 111, B-2440 Geel, Belgium*

<sup>2</sup> *Laboratorio de Metrología de Radiaciones Ionizantes, CIEMAT, Avenida Complutense 40, 28040 Madrid, Spain*

<sup>3</sup> *BNM-CEA/Laboratoire National Henri Becquerel, F-91191 Gif-sur-Yvette Cedex, France*

High-resolution alpha-particle spectrometry was performed to determine the main alpha-particle emission probabilities in the decay of  $^{226}\text{Ra}$ . Thin, homogeneous sources were prepared by electrodeposition on stainless steel disks. Alpha spectra with an energy resolution of 20 keV were obtained in three laboratories and analysed with different deconvolution algorithms. In two set-ups, a magnet system was used to deflect conversion electrons to avoid their coincidental detection with the alpha particles. Spectra taken at close range without a magnet system yielded biased results which cannot be fully compensated by mathematical corrections for coincidence summing. The derived emission probabilities of the three main alpha decays are 94.07 (1) %, 5.93 (1) %, and 0.0059 (15) %, respectively. They are in excellent agreement with calculated values derived from the P( $\gamma$ +ce) decay scheme balance, which solves the existing discrepancy problem with two previous direct measurements published in literature.

Keywords: alpha spectrometry;  $^{226}\text{Ra}$ ; decay data; alpha-particle emission probabilities

---

\* stefaan.pomme@ec.europa.eu; tel. +32 (0)14 571 289; fax +32 (0)14 571 864



## 1 Introduction

Naturally Occurring Radioactive Materials (NORM) are materials found in the environment containing naturally-occurring radioactive isotopes, which when processed by industry may lead to enhanced radiation levels. NORM waste will not decay to insignificant levels within a 'reasonable' time, making it a potential hazard for increased human radiation exposure. Specifically,  $^{226}\text{Ra}$  is present in NORM waste originating from many activities such as the phosphate industry, oil and gas production, and rare earth element and coal extraction. Its affinity to the aqueous phase results in elevated activity concentrations in the water streams used during oil and gas production and in the deposits of the inner parts of the used pipes (IOGP, 2016). Solid residues containing more than 10 Bq/g of  $^{226}\text{Ra}_{\text{eq}}$  (i.e.,  $^{226}\text{Ra}$  in equilibrium with its short-lived progeny  $^{222}\text{Rn}$ ,  $^{218}\text{Po}$ ,  $^{214}\text{Pb}$ ,  $^{214}\text{Bi}$ , and  $^{214}\text{Po}$ ) are considered as radioactive waste. Activity concentrations of members of the  $^{238}\text{U}$  and  $^{232}\text{Th}$  decay series below 1 kBq/kg are exempted according to the Basic Safety standards of the European Union (EURATOM, 2013) and of the IAEA (2014).

A research project on metrology of NORM was conducted within the JRP IND57 'MetroNORM' under the auspices of the European Metrology Research Project (EMRP). One of the aims was the improvement of our knowledge of the decay characteristics of typical NORM nuclides. Radioanalytical procedures applied for the identification of NORM nuclides and quantification of their activity concentrations require reference materials, decay data and analysis methods for accurate results. In this context, the characteristics of alpha decay of  $^{226}\text{Ra}$  have been investigated in this work for possible improvement or validation of previously published alpha emission probabilities.

$^{226}\text{Ra}$  is an alpha-particle emitter with a half-life of 1600 (7) a (DDEP, 2004-2013; LNHB, 2015). It decays to the stable nuclide  $^{206}\text{Pb}$  through a chain of thirteen alpha and beta emitters, as shown in the decay scheme in [Fig. 1](#). The alpha-particle emission probabilities have been measured twice in the past. Bastin-Scoffier et al. (1963) measured a  $^{226}\text{Ra}$  source on  $\text{Al}_2\text{O}_3$  foil in a magnetic spectrograph. The uncertainties on the two main alpha emission probabilities were not provided. La Mont et al. (2001) performed spectrometry measurements of an electrodeposited source with a  $50\text{ mm}^2$  silicon detector, altering the geometric efficiency of the system by varying the source-detector distance. In that way, true coincidence summing effects could be quantified and corrected for in the determined alpha-

emission probabilities,  $P_\alpha$ . Their results and the evaluated  $P_\alpha$  values recommended by the DDEP (2004-2013) are shown in **Table 1**. The measured  $P_\alpha$  values of the main peaks differ by 0.61% in absolute numbers, which is equivalent to a relative difference of 6.5% and 10% on the first and second peak, respectively. The DDEP values, derived from the P( $\gamma$ +ce) decay scheme balance, are intermediate.

The discrepancies between measured and calculated  $P_\alpha$  values of an important NORM nuclide as  $^{226}\text{Ra}$  necessitate new accurate direct measurement of the alpha-emission probabilities. This paper reports on such experimental work through high-resolution alpha-particle spectrometry performed in three laboratories, yielding accurate  $P_\alpha$  and uncertainty values for the three main peaks and the essential confirmation of the validity of the established decay scheme (DDEP, 2004-2013).

## 2 Experiment

### 2.1 *Source preparation*

Thin, homogenous  $^{226}\text{Ra}$  sources for alpha spectrometry were prepared by electrodeposition at CIEMAT following the method by Crespo and Jiménez (1997), which is a modification to the method applied by Alvarado et al. (1995). The deposition was performed onto mirror-polished stainless steel disks of 2.5 cm diameter and 1 mm thickness. The disk acted as cathode in the electrolysis cell. The anode was a platinum wire of 1 mm diameter, folded at the base into spiral shape for creating a homogenous electric field between anode and cathode in the solution. The electrolyte was a 0.17 M ammonium oxalate solution containing 150  $\mu\text{g}$  to 300  $\mu\text{g}$  platinum. Its pH was adjusted to 2.6 with concentrated nitric acid. The electrodeposition was carried out at 600 mA for 90 minutes.

### 2.2 *Alpha spectrometry at JRC*

The alpha spectrometry set-ups in use at JRC have been described by Pommé and Sibbens (2008). The measurement set-up comprises a cuboid source chamber with a sliding source mount and on top a cylindrical distance tube housing a passivated planar ion-implanted silicon detector. Both parts are operated under vacuum, but can be separated by a vacuum lock to maintain vacuum at the detector side during source changes. A sliding piston built on a vacuum feedthrough at the bottom of the chamber allows moving the source up to 100 mm closer to the detector, thus varying the solid angle subtended by the detector. The

preamplifier housing, external to the vacuum chamber, is stabilised in temperature by circulating water from a thermostatic bath around the housing, to reduce peak shift during long measurement campaigns.

The  $^{226}\text{Ra}$  spectrometry measurements were performed with two PIPS<sup>®</sup> detectors of 150 mm<sup>2</sup> and 300 mm<sup>2</sup> active areas, respectively. The solid angle subtended by the detector ranged from 0.9 % to 2.9 % of  $4\pi$  sr. A thin metal baffle of 14.6 mm inner diameter was placed between the source and detector to reduce the detection of scattered alpha-particles and radioactive decay from contaminants in the inner walls of the chamber. A magnet system, designed and constructed by Paepen et al. (2014) at JRC, has been placed on top of the source mount to deflect conversion electrons away from the detector. Using a spacing of 20 mm between the magnets, most of the electron detections can be suppressed up to electron energies of at least 320 keV. This is demonstrated in Fig. 2 by means of spectra of a  $^{237}\text{Np}$  point source acquired with and without a magnet. It shows the detrimental impact of summing effects on the shape of the alpha spectrum and the elimination of conversion electron peaks around 196, 225 and 292-308 keV from the daughter nuclide  $^{233}\text{Pa}$  decaying to  $^{233}\text{U}$  (see also Paepen et al., 2014). The magnet system is assumed to be equally effective for the <190 keV conversion electrons of  $^{222}\text{Rn}$  emitted after the  $^{226}\text{Ra}$  decay.

The  $^{226}\text{Ra}$  measurement campaign lasted one year. The alpha spectra were acquired in daily cycles and subsequently summed through software which automatically corrects for electronic gain drift (Pommé and Sibbens, 2004a; 2004b; 2008). This resulted in five composite spectra with a total number of counts in the  $^{226}\text{Ra}$  alpha peaks ranging from  $6\times 10^6$  to  $1.5\times 10^7$ . Some experimental characteristics are summarised in Table 2. The  $^{226}\text{Ra}$  sources were covered with VYNS foils to avoid contamination, which limited the energy resolution of the peaks to 20 keV (FWHM). Nevertheless, the foil coverage did not prevent recoil atoms from escaping the source (see section 2.5).

The alpha spectra were fitted with the deconvolution software 'BEST' (Pommé and Caro Marroyo, 2015), which applies the commonly used convolutions of a Gaussian with exponentials (Bortels and Collaers, 1987) with the advanced option of implementing up to 10 left-handed and 4 right-handed exponentials if the spectral quality allows perfecting the line shape to the extreme. For the  $^{226}\text{Ra}$  spectra, seven left-handed exponentials were used. The peaks of the daughter nuclides  $^{214}\text{Po}$ ,  $^{218}\text{Po}$ ,  $^{222}\text{Rn}$ , and  $^{210}\text{Po}$  were fitted as well, to determine

the interference of their low-energy tailing in the  $^{226}\text{Ra}$  spectrum. A measured spectrum and the corresponding fit are shown in Fig. 3.

### 2.3 *Alpha spectrometry at CIEMAT*

The measurement setup at CIEMAT was similar to those used at JRC (section 2.2), since they were based on a common design. Two analog electronics setups were used dependent on the detector size, composed by preamplifiers (with Peltier temperature stabilisation), spectroscopy amplifiers and successive-approximation analog-to-digital converters. Given the low activity of the source, long counting times were needed and peak shift due to electronics had to be corrected for. Individual spectra were taken in daily cycles and combined following a procedure based on the Fourier Transform (Rubio Montero and García-Toraño, 2007). Thus, four sum spectra were obtained from measurement series using silicon detectors with three sizes of active area:  $50\text{ mm}^2$ ,  $150\text{ mm}^2$  (2 series) and  $450\text{ mm}^2$ . The relative solid angles of the measurements varied between 0.5% and 5%. The total number of counts in the region of interest varied between  $0.87 \times 10^6$  for the spectrum measured with the smaller detector, to  $8.3 \times 10^6$  with the larger detector. An overview of experimental characteristics of the four spectra is given in Table 3.

The  $^{226}\text{Ra}$  source was covered with a thin VYNS foil to minimise escape of recoil atoms. Due to the source thickness and the cover foil, the obtained energy resolution in all spectra was limited to about 20 keV (FWHM). Peak-to-tail ratios, however, were dependent on the detector size and solid angle applied for a particular spectrum. Whereas a combination of magnets and diaphragms was used to reduce coincidence-summing events, the results from spectral deconvolution analyses still had to be corrected mathematically for residual effects.

Spectral fitting at CIEMAT was carried out using the computer code 'ALPACA' (García-Toraño, 1996). The code uses an analytical expression to model the peak shape and implements a combination of Powell and Newton–Raphson methods to obtain the peak intensities through the minimisation of the chi-square statistics.

### 2.4 *Alpha spectrometry at LNHB*

The spectrometry set-up at LNHB was not equipped with a thermostatic bath for stabilisation of electronics nor a magnet system to deflect conversion electrons and there was no software

for off-line spectral alignment. The measurements performed in less than perfect conditions demonstrated two pitfalls which make this type of measurements difficult: (1) gain shift and (2) summing effects (Pommé, 2015). The requirement of good resolution implies the use of thin sources with relatively low activity, which necessitates long measurement times. However, without special measures for (electronic and off-line) peak stabilisation, the spectral shift has a negative impact on the spectral peak shape and resolution. On the other hand, applying short source-detector distance to gain in statistical accuracy over a shorter measurement time leads to distortions of the alpha spectra through true coincidence effects. Without magnet system, these effects can only be avoided by lowering the effective solid angle. These dilemmas have also been encountered with alpha spectrometry of long-lived nuclides such as  $^{238}\text{U}$  (Pommé et al., 2014) and  $^{236}\text{U}$  (Marouli et al., 2014).

### 2.5 $^{226}\text{Ra}_{\text{eq}}$ spectrum and satellite peaks

A typical spectrum of the  $^{226}\text{Ra}_{\text{eq}}$  decay series and the corresponding background spectrum obtained at the JRC are shown in Fig. 4. The alpha peaks of  $^{226}\text{Ra}$  reside on the low-energy tail of alpha particles emitted by the daughter nuclides (mainly  $^{222}\text{Rn}$  and  $^{218,214,210}\text{Po}$ ). The high-energy side of the daughter peaks exhibit a bump or 'satellite peak' which is caused by the decay of recoiled atoms. The  $^{226}\text{Ra}$  sources were covered by a VYNS foil, but this was not sufficient to prevent recoil atoms from escaping the source. This is confirmed by the background spectrum acquired shortly after the  $^{226}\text{Ra}$  source was removed from the chamber: recoil peaks appear shifted towards a higher energy compared to the alpha peaks generated directly from the source, i.e. approximately by 21 keV ( $^{222}\text{Rn}$  @ 5489 keV), 35 keV ( $^{218}\text{Po}$  @ 6002 keV), 38 keV ( $^{214}\text{Po}$  @ 7686 keV), and 32 keV ( $^{210}\text{Po}$  @ 5304 keV) respectively.

An explanation to the phenomenon of satellite peaks in decay series measurements has been proposed by Nylandsted Larsen et al. (1984). Atoms undergoing alpha decay can recoil into the surface layer of the silicon detector. Subsequent decay of the daughter nuclide takes place inside the detector and a part of the recoil energy of the atom (the fraction giving rise to ionisations in the depletion zone) is detected in coincidence with the alpha particle. The energy difference between the recoil peak and the corresponding  $\alpha$  peak therefore depends on the recoil energy, but may also increase when going further in the decay series due to recoils knocking themselves deeper into the depletion zone. Similar observations have been made recently in measurements of the  $^{230}\text{U}$  (Marouli et al., 2012) and  $^{225}\text{Ac}$  (Marouli et al., 2013) decay series.

Apart from raising the background level in the chamber and distorting the daughter peak shapes, the satellite peaks did not interfere with the determination of the  $^{226}\text{Ra}$  alpha emission probabilities, because the parent nuclide peaks are not affected by recoils.

## 2.6 True coincidence effects

The two main excited states of  $^{222}\text{Rn}$  fed by  $^{226}\text{Ra}$  alpha decay have a significant probability for de-excitation through the emission of internal conversion electrons (ICE). The first excited level at 186 keV (fed by alpha transition  $\alpha_1$ ) has a total conversion coefficient of  $\alpha_T = 0.677$  (10), mostly ejecting L shell electrons ( $\alpha_L = 0.360$  (5)) and to a lesser extent K ( $\alpha_K = 0.190$  (3)) and M ( $\alpha_M = 0.0963$  (14)) shell electrons (DDEP, 2004-2013). The ICE energies of the 186 keV transition vary between 87.8 keV (K) and 186 keV (N). The 2<sup>nd</sup> excited level at 448 keV (fed by alpha transition  $\alpha_2$ ) has a gamma transition of 262 keV to the 1<sup>st</sup> level, with a total conversion coefficient of  $\alpha_T = 0.209$  (4), mostly ejecting K ( $\alpha_K = 0.0923$  (14)) and L shell electrons ( $\alpha_L = 0.0868$  (14)) and to a lesser extent M shell electrons ( $\alpha_M = 0.0230$  (4)) (DDEP, 2004-2013). The  $\alpha_2$  alpha particles can be detected in coincidence with an ICE of the 186 keV transition, the 262 keV transition, or both.

When measuring at a 3% solid angle, the probability of measuring the alpha particle  $\alpha_1$  in coincidence with an ICE is 1.2 %. The combined energy of both particles results in summing-out from the  $\alpha_1$  peak and summing-in into the  $\alpha_0$  peak (of the transition to the ground level). One would expect that this can be solved with a mathematical correction factor, but there is an additional effect in play: the coincident signal generally ends up in the low-energy tail of the main peak, thus distorting the spectral shape parameters of the fitted peaks. This results in an artificial raise of the tailing part of the  $\alpha_0$  peak, thus affecting the spectral deconvolution such that a part of the  $\alpha_1$  peak is wrongly assigned to the low-energy tail of the  $\alpha_0$  peak. The effect of spectral distortion on the calculated relative emission probabilities is a multiple of the statistically expected summing corrections (Pommé et al., 2014; Marouli et al., 2014; Pommé, 2015).

X rays are emitted with energies from 10 keV to 17 keV (XL) and from 80 keV to 98 keV (XK), with emission probabilities of 0.807 (14) % and 0.65 (1) %, respectively. This is comparably lower than the 2.407 (36) % emission probability of ICE of the 186 keV transition. The photoabsorption probability of the XL and XK rays in 300  $\mu\text{m}$  Si, corresponding to the depletion depth of the detector, is approximately 10-35% and 0.02-

0.07%, respectively, depending on their energy. Coincident signals with XL photons would end up at the high end of the alpha peak, whereas coincidences with the XK signals would contribute to the tail of a higher-energy alpha peak. The summing-out probability from the  $\alpha_1$  peak due to XK photons (incl. Compton interactions) in a configuration covering less than 3% of  $4\pi$  solid angle should be negligible (<0.001%), whereas the effect of the low-energy XL photons (<0.05%) on the spectral deconvolution is unclear at first instance.

Coincidence effects are not negligible when aiming at 0.01% accuracy. The effect of electrons can be greatly reduced with magnet systems. The residual coincidence effects from electrons and X rays can be further reduced by measuring at different distances and extrapolating the obtained emission probabilities to a result at infinite distance.

### 3 Measurement results

Five sum spectra at JRC and four at CIEMAT have been analysed and their characteristics are summarised in Tables 2 and 3, respectively. In Fig. 5, a zoom-in is shown of the fit of the  $^{226}\text{Ra}$  peaks and the underlying tailing of the daughter peaks for a spectrum obtained at the JRC. Fig. 6 shows a measured and fitted spectrum obtained at CIEMAT, in which the tailing of the daughter peaks has been subtracted from the spectrum prior to the fitting of the two main  $^{226}\text{Ra}$  peaks. The peaks at 4784 keV ( $\alpha_0$ ), 4601 keV ( $\alpha_1$ ) and 4340 keV ( $\alpha_2$ ) are well separated in energy and the two main peaks could be fitted accurately. For four spectra, the  $\alpha_2$  peak could not be fitted because an insufficient amount of counts were collected to reach the required statistical accuracy. In these cases, the recommended (DDEP, 2004-2013)  $\alpha_2$  emission probability derived from  $\gamma$ -ray spectrometry was applied as a fixed parameter in the spectral deconvolution. The alpha emission probabilities were calculated as the ratio of the number of counts in the individual peaks to the sum of all alpha peak areas of  $^{226}\text{Ra}$ .

At the JRC, the fitted intensities of the two main peaks – 94.08 % and 5.92 %, respectively – remained quasi-invariable to changes in the geometrical efficiency ranging between  $G=0.9$  % and 2.9 %. This confirms the effectiveness of the magnet system in deflecting the ICE and the low impact of coincidence effects between the alpha particles and the X rays. In spite of the use of magnets at CIEMAT, some residual coincidence effect was visible when varying the solid angle between 0.5 % and 5.4 % of  $4\pi$ . At the lowest geometry factor,  $G = 0.5$  %, the  $P_\alpha$  values of 94.08 % and 5.92 % were confirmed, whereas at  $G = 5.4$  % the results deviated by

10 times the statistical standard deviation. An extrapolation procedure was applied for  $P_\alpha$  values as a function of the geometry factor and the intercept values at  $G = 0$  provided the optimal results. The linear extrapolation curves are presented in [Fig. 7](#). The final results – 94.06 % and 5.94 % – are very close to the ones obtained at the JRC, even though different sources, experimental equipment, line shape models, and fitting software were used.

The measurements at LNHB, performed at short source-detector distance ( $G=6\%$ ), exemplified the detrimental effect of coincidence summing between conversion electrons and alpha particles on the determination of alpha emission probabilities, even when mathematical corrections are applied. The LNHB results for the alpha emission intensities for the major peaks were 94.55 (4) %, 5.44 (4) % and 0.007 (6) %, similar to the results of Bastin-Scoffier et al. (1963) in Table 1. When mathematical corrections (see e.g. (Sibbens et al.,2010)) were applied to account for the coincidence summing effects, the new emission intensities were calculated as 94.49 (4)%, 5.51 (4)% and 0.007 (6)%. They were not included in the final result of this work due to the unfavourable measurement conditions.

The final  $P_\alpha$  values – 94.07 %, 5.93 % and 0.0059 % – were calculated from a mean between the JRC and CIEMAT results. They are in excellent agreement with the DDEP values, 94.04 (4) %, 5.95 (4) % and 0.0066 (22) %, but discrepant with the direct measurement results of Bastin-Scoffier et al. (1963) and LaMont et al. (2001) in Table 1.

## 4 Uncertainties

### 4.1 Shortcut formula

Typical uncertainty components of the emission probabilities include statistical uncertainty of the peak areas of interest ( $A_k$ ) as well as a (tailing) fraction of the interfering peaks ( $A_k^t$ ), summing effects and spectral distortions of the spectra due to true coincidences, and imperfections in the modelling of alpha spectra ( $A_k^f$ ). Errors on the area determination of interfering peaks induce anti-correlated errors in the peak of interest, which increases uncertainty. Normalisation of the total area of  $^{226}\text{Ra}$  peaks to 100 %, on the other hand, reduces the relative uncertainty on  $P_k=A_k/\Sigma A_k$  through correlation, where  $P_k$  is the emission probability of the peak  $k$ .

By good approximation, one may ignore the different propagation factors and calculate the statistical uncertainty for each peak through the standard uncertainties on their peak areas via

$$\sigma(A_k) = \sqrt{A_k + 2 \cdot (A_k^t + A_k^f)} \quad (1)$$

and the propagation formula for independent uncertainties (Pommé, 2015)

$$\sigma^2(P_k) = P_k^2(1 - P_k)^2 \left( \frac{\sigma^2(A_k)}{A_k^2} + \frac{\sigma^2(\sum_{i \neq k} A_i)}{(\sum_{i \neq k} A_i)^2} \right) \quad (2)$$

However, to provide additional transparency in the uncertainty budget, a more detailed account of the main uncertainty components and their propagation will be given below for the JRC spectrum measured at 2.9 % geometrical efficiency.

#### 4.2 Poisson uncertainty of peak area

Firstly, uncorrelated statistical uncertainties in the peak areas are considered. The Poisson uncertainties on the peak areas propagate to the  $P_k$  via Eq. 2. In a spectrum with  $\Sigma A_i = 14,902,122$  counts and  $A_0=14,019,292$ ,  $A_1 = 881777$ ,  $A_2 = 905$  the standard uncertainty on the emission probability of the main peak,  $P_0$ , due to Poisson statistics is

$$\begin{aligned} \sigma(P_0) &= (1 - P_0)P_0 \sqrt{\frac{1}{A_0} + \frac{1}{A_1 + A_2}} \\ &= (94.076\%)(5.924\%) \left( \frac{1}{14,019,292} + \frac{1}{882,830} \right)^{0.5} \approx 0.006\% \end{aligned} \quad (3)$$

The same equation can be applied mutatis mutandis for  $P_1$  and  $P_2$ . The standard uncertainty on  $P_1$  is also 0.006 % due to strong anti-correlation with  $P_0$ , and the statistical uncertainty on  $P_2$  is 0.0002 %.

The systematic error due to modelling of the central peak area is comparably small, considering that the difference between the fitted and measured count integrals in the central peak regions of  $\alpha_0$  and  $\alpha_1$  is below 0.0002 % and 0.02 %, respectively. Propagation of a

hypothetical 0.02 % relative error on the peak modelling yields a standard uncertainty of 0.0016%, 0.0016 % and 0.0000017 % on  $P_0$ ,  $P_1$ , and  $P_2$ , respectively.

### 4.3 Interference of $^{226}\text{Ra}$ peaks

The  $^{226}\text{Ra}$  peaks interfere with each other through tailing. The uncertainty due to tailing from the  $^{226}\text{Ra}$  peaks may create an anti-correlation which increases the uncertainty: if the tailing of the  $\alpha_0$  peak is overestimated, the area of the  $\alpha_1$  and  $\alpha_2$  peaks may be underestimated and the effect is felt twice in the ratio of the peak areas. The anti-correlated uncertainties are propagated through (Pommé, 2015)

$$\sigma^2(P_k) = \left( \frac{\sigma^2(A_k)}{(\sum_i A_i)^2} \right) \quad (4)$$

For an estimate of the interference from tailing on a specific peak, only the channels within about  $2 \times \text{FWHM}$  of the peak top have been considered, since this is the decisive region where 90% of the counts are concentrated and where the peak amplitude is determined. Underneath the central region of the  $\alpha_1$  peak a tailing area of 5787 counts from the  $\alpha_0$  peak has been fitted, to which 10% can be added to estimate the 'total interference' on the full  $\alpha_1$  peak. Underneath the central region of the  $\alpha_2$  peak, there are 1136 counts from the  $\alpha_0$  tailing and 172 counts from the  $\alpha_1$  tailing. The square roots of these areas are taken as additional uncertainty component for the interfering peaks, and twice for the interfered peaks for which these areas have been 'subtracted'.

The systematic uncertainty on the fitted tailing is considered small since the whole spectrum in between peaks in Fig. 3 is well represented by the same tailing function applied to all peaks. To the Poisson uncertainty, a systematic uncertainty of 0.1% of the tailing area has been added. Applying Eq. 3 gives the following absolute uncertainty estimates for interference by  $^{226}\text{Ra}$  peaks:

$$\sigma(P_0) = \left( \frac{\sqrt{6420+1253}}{14,902,122} \right) = 0.0006\% \quad (5)$$

$$\sigma(P_1) = \left( \frac{\sqrt{2 \times 6420 + 190}}{14,902,122} \right) = 0.0008\% \quad (6)$$

$$\sigma(P_2) = \left( \frac{\sqrt{2 \times (1253 + 190)}}{14,902,122} \right) = 0.0004\% \quad (7)$$

#### 4.4 Tailing from daughter peaks

Besides the mutual interference of  $^{226}\text{Ra}$  peaks, there is an even larger interference by the tailing of the daughter peaks in the high-energy part of the spectrum. Their area underneath the central part of the  $\alpha_0$ ,  $\alpha_1$ , and  $\alpha_2$  peaks ( $2 \times \text{FWHM}$ ) is 10976, 6819, and 3556 counts respectively. Adding again about 10 % to the areas, the propagation via Eq. 2 of the Poisson uncertainties on  $P_0$ ,  $P_1$ , and  $P_2$ , is 0.001 %, 0.0008 %, and 0.006 %, respectively. An example calculation is shown for  $P_0$

$$\sigma(P_0) = (94.076\%)(5.924\%) \left( \frac{2 \times 12098}{14,019,292^2} + \frac{2 \times (7521 + 3918)}{882830} \right)^{0.5} \approx 0.001\% \quad (8)$$

A hypothetical systematic error of 0.1 % in the tailing propagates to 0.0001 %-0.0004 % uncertainty, since the correlation reduces the effect on the peak area ratios.

#### 4.5 Spectral distortion

By combining several spectra, the statistical uncertainties are further reduced and systematic errors gain importance. A significant uncertainty component is the spectral distortion caused by coincidental detection of alpha particles with electrons and X-rays. The induced error on the emission probabilities can be estimated from the dependence of the measurement results on the solid angle of the measurement configuration.

At the JRC, the standard deviation on  $P_0$  and  $P_1$  among the four measurements between 0.9% and 2.9 % geometrical efficiency is 0.002 %, which is an order of magnitude smaller than the statistical uncertainty in three of the spectra. Therefore, no significant slope can be observed due to summing effects. An uncertainty of 0.007 % for the two main peaks and 0.0007% for the  $\alpha_2$  peak have been assigned to cover possible residual effects.

At CIEMAT, the two main emission probabilities show a slope of about 0.045 % with every 1 % change in geometrical efficiency. An uncertainty of 0.02 % on the extrapolated value was estimated.

For the final value, a power-moderated mean (Pommé and Keightley, 2015) was taken of the JRC and CIEMAT mean values with their uncertainties. The result is presented in Table 1.

## **5 Conclusions**

The three main alpha-particle emission probabilities of  $^{226}\text{Ra}$  have been measured by high-resolution alpha-particle spectrometry at three laboratories. The sources were produced by electrodeposition to offer good energy resolution. The derived emission probabilities of the three main alpha decays are 94.07 (1) %, 5.93 (1) %, and 0.0059 (15) %, respectively. They are in excellent agreement with calculated values derived from the  $P(\gamma+ce)$  decay scheme balance, which solves the existing discrepancy problem with two previous direct measurements published in literature.

## References

Alvarado, J. S., Orlandini, K. A., Erickson, M. D., 1995. Rapid determination of radium isotopes by alpha spectrometry. *J. Radioanal. Nucl. Chem.* 194, 163–172.

Bastin-Scoffier, G., Leang, C. F., Walen, R. J., 1963. Spectrographie  $\alpha$  de  $^{226}\text{Ra}$  et niveaux des Rn de A pair. *Le Journal de Physique* 24, 854–856.

Crespo, M. T., Jiménez, A. S., 1997. On the determination of radium by alpha spectrometry. *J. Radioanal. Nucl. Chem.* 221, 149–152.

DDEP, 2004-2013. Table of Radionuclides, Vol. 1-7, Monographie BIPM-5 BIPM, Sèvres, website: [http://www.nucleide.org/DDEP\\_WG/DDEPdata.htm](http://www.nucleide.org/DDEP_WG/DDEPdata.htm)

EURATOM, 2013. Council Directive 2013/59/EURATOM of 5 December 2013 laying down basic safety standards for protection against the dangers arising from exposure to ionising radiation, and repealing Directives 89/618/Euratom, 90/641/Euratom, 96/29/Euratom, 97/43/Euratom and 2003/122/Euratom, OJ L 13, 17.01.2014.

García-Toraño, E., 1996. A comparative study of minimization methods in the fitting of alpha-particle spectra. *Nucl. Instr. Meth. Phys. Res.* 369, 609–612.

IAEA, International Atomic Energy Authority, 2014. Radiation protection and safety of radiation sources: international basic safety standards. IAEA Safety Standards Series No. GSR Part 3, STI/PUB/1578, ISBN 978–92–0–135310–8

IOGP, International Association of Oil & Gas Producers, 2016. Managing naturally occurring radioactive material (NORM) in the oil and gas industry. Report 412.

LaMont, S. P., Gehrke, R. J., Glover, S. E., Filby, R. H., 2001. Precise determination of the intensity of  $^{226}\text{Ra}$  alpha decay to the 186 keV excited state. *J. Radioanal. Nucl. Chem* 248, 247–253.

LNHB, Laboratoire National Henri Becquerel, 2015. Mini Table of Radionuclides. ISBN: 978-2-7598-1198-4.

Marouli, M., Pommé, S., Paepen, J., Van Ammel, R., Jobbágy, V., Dirican, A., Suliman, G., Stroh, H., Apostolidis, C., Abbas, K., Morgenstern, A., 2012. High-resolution alpha-particle spectrometry of the  $^{230}\text{U}$  decay series. *Appl. Radiat. Isot.* 70, 2270–2274.

Marouli, M., Suliman, G., Pommé, S., Van Ammel, R., Jobbágy, V., Stroh, H., Dikmen, H., Paepen, J., Dirican, A., Bruchertseifer, F., Apostolidis, C., Morgenstern, A., 2013. Decay data measurements on  $^{213}\text{Bi}$  using recoil atoms. *Appl. Radiat. Isot.* 74, 123–127.

Marouli, M., Pommé, S., Jobbágy, V., Van Ammel, R., Paepen, J., Stroh, H., Benedik, L., 2014. Alpha-particle emission probabilities of  $^{236}\text{U}$  obtained by alpha spectrometry. *Appl. Radiat. Isot.* 87, 292–296.

Nylandsted Larsen, A., Bortels, G., Denecke, B., 1984. Satellite peaks in high-resolution alpha-particle spectra of decay-chain members measured with silicon surface-barrier detectors, *Nucl. Instr. Meth. Phys. Res.* 219, 339–346.

Paepen, J., Dirican, A., Marouli, M., Pommé, S., Van Ammel, R., Stroh, H., 2014. A magnet system for the suppression of conversion electrons in alpha spectrometry. *Appl. Radiat. Isot.* 87, 320–324.

Pommé, S., Sibbens, G., 2004a. Concept for an off-line gain stabilisation method. *Appl. Radiat. Isot.* 60, 151–154.

Pommé, S., Sibbens, G., 2004b. A new off-line gain stabilisation method applied to alpha-particle spectrometry. In: *Advanced Mathematical and Computational Tools in Metrology VI*, ed. P. Ciarlini, M. G. Cox, F. Pavese, G. B. Rossi, Series on Advances in Mathematics for Applied Sciences – Vol. 66 (World Scientific Publishing Company, 2004) pp. 327–329.

Pommé, S., Sibbens, G., 2008. Alpha-particle counting and spectrometry in a primary standardisation laboratory. *Acta Chim. Slov.* 55, 111–119.

Pommé, S., García-Toraño, E., Marouli, M., Crespo, M. T., Jobbágy, V., Van Ammel, R., Paepen, J., Stroh, H., 2014. High-resolution alpha-particle spectrometry of  $^{238}\text{U}$ . *Appl. Radiat. Isot.* 87, 315–319.

Pommé, S., 2015. Typical uncertainties in alpha-particle spectrometry. *Metrologia* 52, S146–S155.

Pommé, S., Marroyo, B. C., 2015. Improved peak shape fitting in alpha spectra. *Appl. Radiat. Isot.* 96, 148–153.

Pommé, S., Keighley, J., 2015. Determination of a reference value and its uncertainty through a power-moderated mean. *Metrologia* 52, S200–S212.

Rubio Montero, M. P., García-Toraño, E., 2007. Use of discrete Fourier transform to sum spectra in measurements with long counting times. *Nucl. Instrum. Methods Phys. Res. Sect. A* 577, 715–718.

Sibbens, G., Pommé, S., Altizoglou, T., García-Torano, E., Janßen, H., Dersch, R., Ott, O., Martín Sánchez, A., Rubio Montero, M.P., Loidl, M., Coron, N., de Marcillac, P., Semkow, T. M., 2010. Alpha-particle emission probabilities in the decay of  $^{240}\text{Pu}$ . *Appl. Radiat. Isot.* 68, 1459-1466.

Table 1: Measured and evaluated alpha-particle emission probabilities ( $P_\alpha$ ) in the decay of  $^{226}\text{Ra}$ .

Comment / Reference	$\alpha_0$	$\alpha_1$	$\alpha_2$
<b><math>^{226}\text{Ra} - P_\alpha</math> (%)</b>			
G. Bastin-Scoffier et al. (1963)	94.45	5.55	0.0065
S. LaMont et al. (2001)	93.84 (11)	6.16 (3)	
Recommended value (DDEP)	94.038 (40)	5.95 (4)	0.0066 (22)
This work CIEMAT	<b>94.06 (2)</b>	<b>5.94 (2)</b>	<b>0.0052 (15)</b>
This work JRC	<b>94.077 (10)</b>	<b>5.917 (10)</b>	<b>0.0067 (20)</b>
Mean value JRC+CIEMAT	<b>94.07 (1)</b>	<b>5.93 (1)</b>	<b>0.0059 (15)</b>

Table 2: Alpha-particle emission probabilities ( $P_\alpha$ ) in the decay of  $^{226}\text{Ra}$  from five measurements at JRC-Geel.

Measurements		$\alpha_0$	$\alpha_1$	$\alpha_2$
$^{226}\text{Ra}$ source	$\Omega/4\pi$ (%)			
Ra226S1504	0.9	94.078 (20)	5.917 (20)	0.005 (2)
	2.0	94.077 (30)	5.917 (30)	$0.0066 (22)^a$
	2.6	94.075 (35)	5.918 (35)	$0.0066 (22)^a$
	2.9	94.080 (10)	5.914 (10)	0.006 (1)
Ra226MNRA1	2.6	94.064 (25)	5.925 (25)	0.0102 (25)
Weighted mean		<b>94.077 (10)</b>	<b>5.917 (10)</b>	<b>0.0067 (20)</b>

<sup>a</sup> Insufficient counts to fit this peak; the recommended value from DDEP (2004-2013) has been used.

Table 3: Alpha-particle emission probabilities ( $P_\alpha$ ) in the decay of  $^{226}\text{Ra}$  from four measurements at CIEMAT.

Measurements		$\alpha_0$	$\alpha_1$	$\alpha_2$
$^{226}\text{Ra}$ source	$\Omega/4\pi$ (%)			
Ra226S05	0.5	94.08 (2)	5.92 (2)	<i>0.0066(22)<sup>a</sup></i>
	2.0	94.12 (2)	5.90 (2)	0.0046(15)
	2.9	94.21 (2)	5.81 (2)	<i>0.0066(22)<sup>a</sup></i>
	5.4	94.29 (2)	5.75 (2)	0.0037(12)
Extrapolated value		<b>94.06 (2)</b>	<b>5.94 (2)</b>	<b>0.0052(15)</b>

<sup>a</sup> Insufficient counts to fit this peak; the recommended value from DDEP (2004-2013) has been used.

Table 4: Uncertainty budget of the alpha emission probabilities of  $^{226}\text{Ra}$  based on the JRC spectrum at  $G=\Omega/4\pi=2.9\%$ , as described in detail in the text. The uncertainties are absolute standard deviations (not relative uncertainties) expressed in %.

Component	$\alpha_0$	$\alpha_1$	$\alpha_2$
Counting statistics <sup>b</sup>	0.007	0.007	0.0002
Interference $^{226}\text{Ra}$ peaks <sup>c</sup>	0.0006	0.0008	0.0004
Tailing daughter peaks <sup>c</sup>	0.001	0.0008	0.0006
Spectral distortion	0.007	0.007	0.0007
Combined Uncertainty <sup>c</sup>	0.010	0.010	0.001
Correlation matrix ( $\rho$ )			
$\alpha_0$	1		
$\alpha_1$	-1	1	
$\alpha_2$	-1	0.9	1

<sup>b</sup> Includes hypothetical 0.02% uncertainty on the fitted peak areas

<sup>c</sup> Includes hypothetical 0.1% systematic error on the tailing areas

## Figure Captions

Fig. 1: The decay series of  $^{226}\text{Ra}$ .

Fig. 2 : Conversion electron spectra following the decay of  $^{237}\text{Np}$  and  $^{233}\text{Pa}$  (bottom) and the corresponding alpha spectra of  $^{237}\text{Np}$  recorded in the set-up with and without the magnet used for the  $^{226}\text{Ra}$  measurements at JRC.

Fig. 3: Measured and fitted alpha spectrum of  $^{226}\text{Ra}_{\text{eq}}$ .

Fig. 4: Alpha-particle spectra of a  $^{226}\text{Ra}$  source and a background spectrum (shaded area) with decays from recoiled atoms in the detector taken at JRC. The upper graph shows a detailed spectrum in the energy region from 5.05 MeV to 6.1 MeV.

Fig. 5: Alpha-particle spectrum of  $^{226}\text{Ra}$  measured with a 300 mm<sup>2</sup> PIPS<sup>®</sup> detector at JRC, including the fitted  $^{226}\text{Ra}$  peaks and the tailing from the daughter nuclides. The residuals show the difference between measurement and fit in units of one standard deviation of the channel contents.

Fig. 6: Alpha-particle spectrum of  $^{226}\text{Ra}$  measured with a 50 mm<sup>2</sup> PIPS<sup>®</sup> detector at CIEMAT. The fit to the two main peaks are presented. Tailing of the daughter nuclides was previously removed as a part of the fitting process. The residuals show the difference between measurement and fit in units of one standard deviation of the channel contents

Fig. 7: Emission probabilities obtained at CIEMAT for the three major emissions of  $^{226}\text{Ra}$ . Data from the analysis of four spectra are presented as a function of the solid angle of the measurement. Extrapolation to zero solid angle provided the final values which are presented in Table 3.

Fig. 1

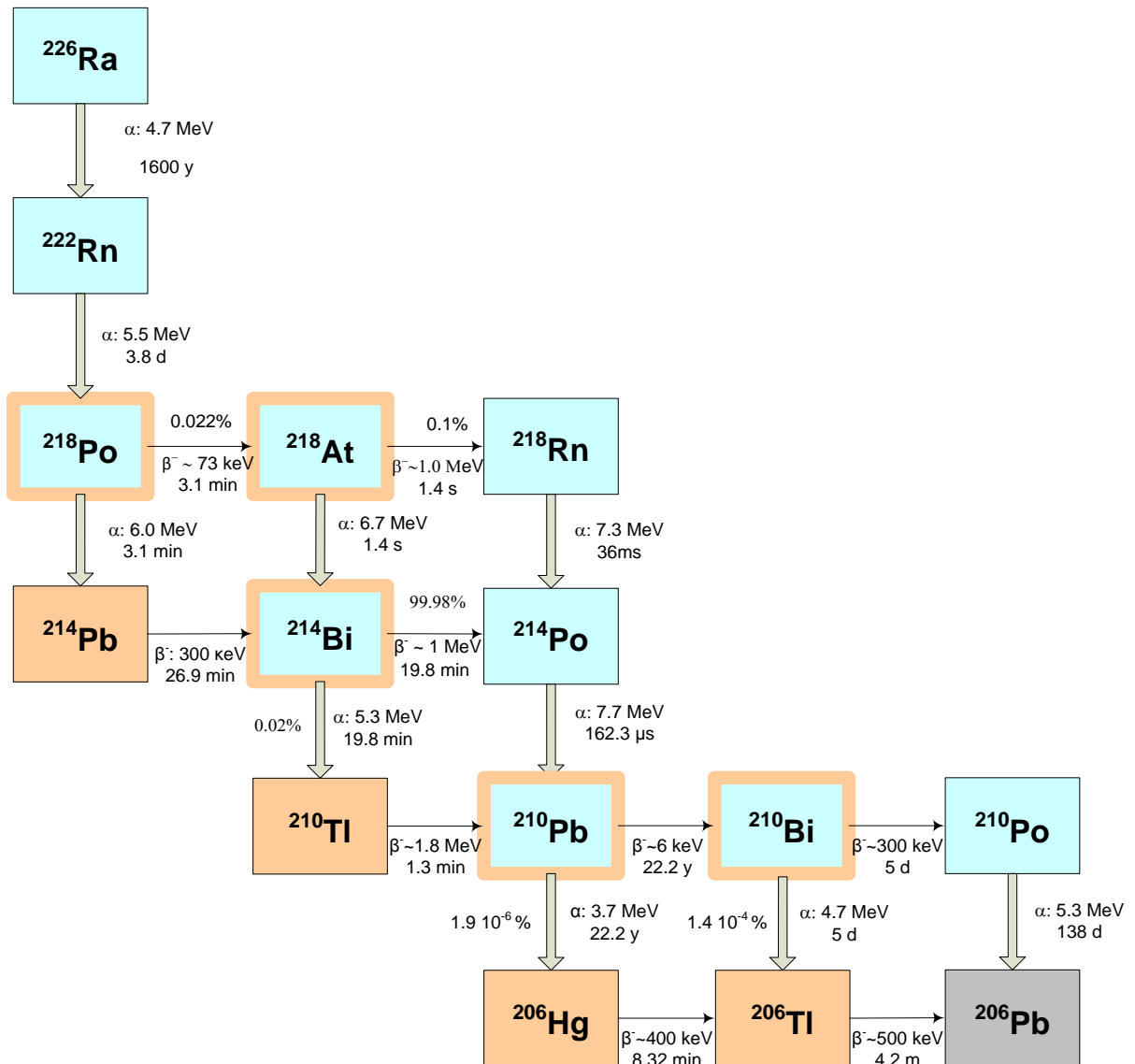


Fig. 2

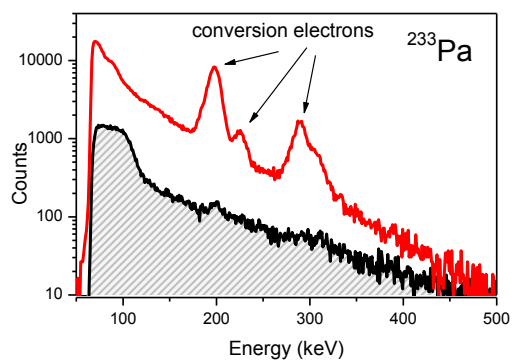
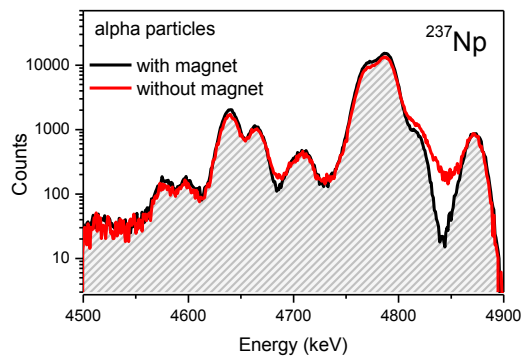


Fig. 3

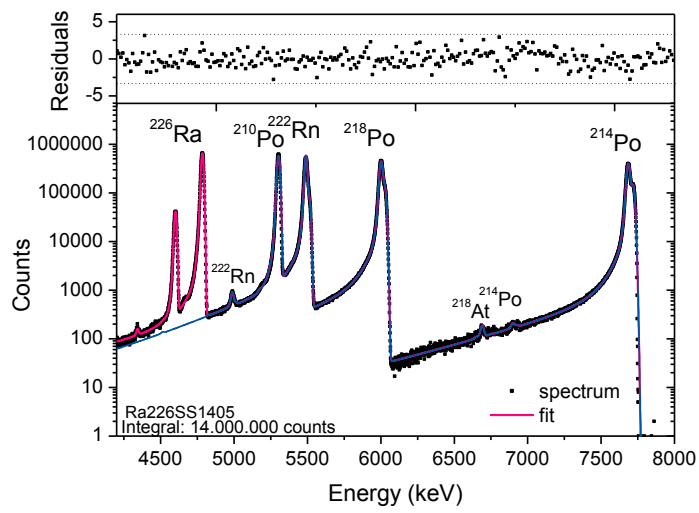


Fig. 4

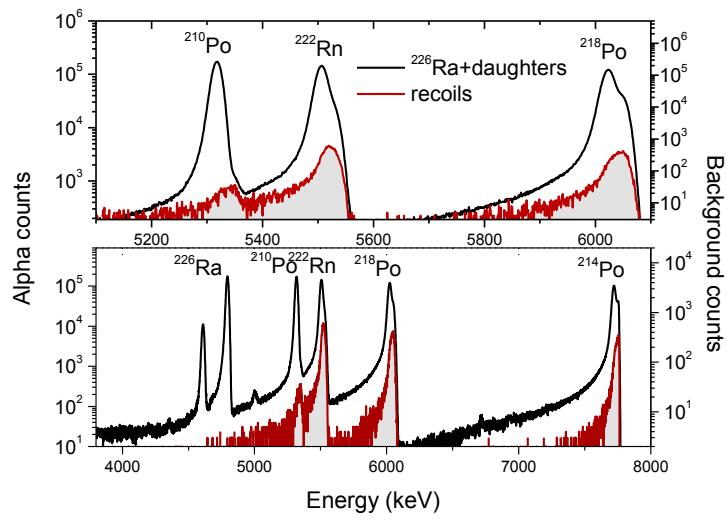


Fig. 5

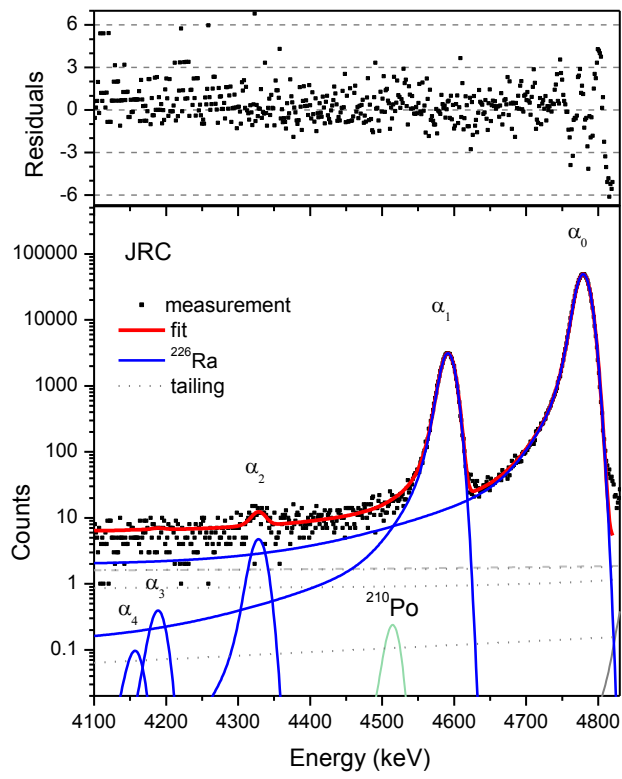


Fig. 6

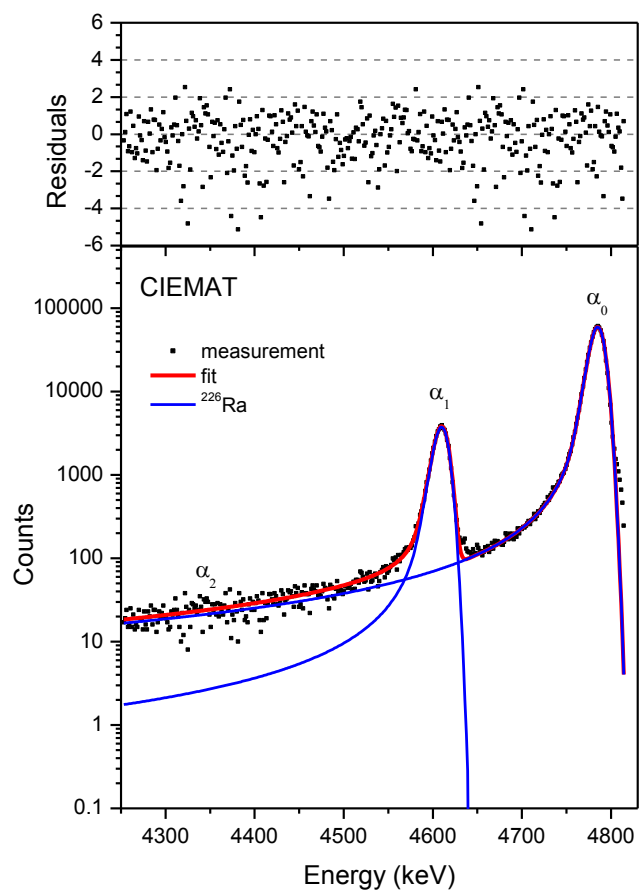


Fig. 7

